LOAD DETECTION OF FUNCTIONALLY GRADED MATERIAL BASED ON COHERENT GRADIENT SENSING METHOD

J. Zhang

School for Engineering of Matter, Transport, and Energy
Arizona State University
Tempe, United States

W. Xu

Department of Engineering Mechanics
Kunming University of Science and Technology
Kunming,China

X. F. Yao*

School of Aerospace
Tsinghua University
Beijing, China

ABSTRACT

Functionally graded material (FGM) has some particular characteristics due to the gradual variation of physical properties. The study on mechanical behavior of FGM is of great research value. In this work, a large scale FGM which filled with small glass spheres has been prepared by gravity assisted casting technique. The elastic material constants in static condition are measured. One optical experimental method, coherent gradient sensing (CGS), is introduced to study the mechanical behavior of FGM which has variation of material property in power-law. The governing equations of CGS which is used to represent the optics-mechanics relation of the singular field near the point of the outside force are derived based on the power-law asymptotic expansion. The experimental result shows this CGS method as a nondestructive methodology can be used to detect the damage in FGM with high accuracy.

Keywords: Functionally graded material, Coherent gradient sensing method, Stress singularity, Optical experimental method.

1. INTRODUCTION

1.1 Functionally Graded Material (FGM)

Micromechanical techniques allow the mechanical behavior of materials to be analyzed through the continuum approximation of heterogeneous microstructures [1, 2]. The variation of microstructural properties leads to variable macroscopic properties [3-6]. Functionally Graded Material (FGM) is a new generation engineering material varying its microstructure over volume with a specific gradient, resulting in corresponding changes in the properties of material (including elasticity modulus, shear modulus and material density). The mechanical response of FGM with spatial gradients in composition and structure is of wide interest in disciplines as diverse as aerospace engineering, tribology, geology, optoelectronics, fracture mechanics, and nanotechnology. FGM which provides a relative change in terms of the properties of materials over the distance and directions can be used for specific function and application. The fundamental design concept is to make a composite material by varying the microstructure from one material to another material with a specific gradient. Different from traditional homogeneous or layer materials, FGM is composed of two or more components of which the weight percentages have gradient variation over volume. Compared with FGM, the traditional homogeneous materials don't have different performance. For the layer materials, there are mismatching issues which will result in residual stress. In contrast with above two kinds of materials, the FGM can provide variable functional per-

* Corresponding author (yxf@mail.tsinghua.edu.cn)

DOI : 10.1017/jmech.2016.114
Copyright © 2016 The Society of Theoretical and Applied Mechanics
https://doi.org/10.1017/jmech.2016.114 Published online by Cambridge University Press

formances at different positions of the material. It also avoids the mismatching between different material properties. The remarkable advantages of FGM enhance the structural strength and provide wider applications than traditional materials. There are multiple methods to prepare the FGM, including vapor deposition method, plasma spraying method, self-propagating high-temperature synthesis method, powder metallurgy method and laser cladding method.

Theoretically, due to the material or geometrical discontinuity the stress and displacement can be infinite and singular at the crack tip or boundary between different materials, from where the mechanical failure may initiate. [7-9] Based on the assumption of the asymptotic expansions of the physical fields near the vertex, the characteristic differential equations with respect to the singularity order are derived from the equilibrium equations. [10] Atkinson and List studied the stress singularity of material with variable mechanical properties. [11] Delale *et al*. found that the stress singularity at crack tip for FGM is similar to that for homogeneous material which has a relation of $\frac{1}{\sqrt{r}}$. [12] Eischen *et al*. validated Delale's observation through theoretical analysis. [13] Huang *et al*. studied the material properties variation of FGM in gradient direction [14] which found the Poisson ratio of FGM has little effect on the stress distribution at crack tip. Chalivendra *et al*. used the power-law function to describe the stress field at crack tip in arbitrary directions. [15] Parameswaran *et al*. used two governing functions, the linear and power-law functions, to describe the FGM material properties, which showed that the power-law function can better express the gradient material properties than linear function. [16] Marur *et al*. first prepared epoxy resin based large scale FGM sample filled with tiny glass balls using gravity assisted casting method. [17] In their study, the elastic modulus and density of their FGM can change as high as three times in gradient direction within 60 mm. Butcher [18] and Parameswaran [19] also made large scale FGM using gravity assisted casting technique and studied stress singularity at crack tip. Based on their study, the fracture toughness of FGM is much higher than layer materials. Yao *et al*. developed glass sphere filled epoxy FGM using gravity assisted casting technique [20-22] and evaluated the deformation and fracture behavior of the FGM.

1.2 Coherent Gradient Sensing (CGS) Method

Damage detection is a complex problem and requires an in-depth understanding of the material characteristics and response under varying load and environmental conditions [23-29]. A significant amount of research has been conducted in this field to enhance the fidelity of damage assessment methodologies, using a wide range of sensors and detection techniques, for both metallic materials and composites [30-34]. However, detecting damage at the microscale is not possible with commercially available sensors. A probable way to approach this problem is through accurate and efficient modeling techniques, which are capable of tracking damage initiation at the microscale and propagation across the length scales. [35-42] Experimentally, the traditional techniques using gauges or other sensors can only obtain stress information at a series of positions. Moreover the gauge or sensor size limits the measurement accuracy of strain and stress at the microscale. A lot of effort has been dedicated to develop the structural health monitoring (SHM) which is critical to both current and future multidisciplinary application. [43-48] The goal of the SHM framework is to detect, quantify, and classify the nature of damage in a structure in order to assess the current state and determine the residual useful life (RUL). As a comprehensive technology, SHM integrates sensors and sensing techniques, damage detection algorithms, and prognosis for accurate estimation of RUL. [49] Compared with traditional mechanical experiment methods, the optical experimental methods are not only a nondestructive measurement but also capable to capture whole stress/strain field information. [50] Therefore the optical mechanical experiment methods as a nondestructive testing method can be widely used to detect stress distribution and monitor local damage precursor.

One optical mechanical experiment method, coherent gradient sensing (CGS) method, has been widely used in stress singularity study. Tippur *et al*. first studied the governing function of stress field using CGS method. [51] Bruck and Rosakis *et al*. discussed the accuracy, error and application of CGS in mechanical experiments and measurements. [52, 53] Lee *et al*. developed a comprehensive model of CGS technology and applied it to wider investigation based on Fourier optics. [54-56] Yao *et al*. used CGS method to study local singularity and fracture characterization of FGM and derived governing equations related to CGS measurement and elastic solution at mode I crack tip in terms of stress, material constants, and fringe order [57-59].

In CGS method, an optical circuit was designed using two parallel optical gratings which are set in a distance (see Fig. 1). This circuit will generate the interference fringes which can be observed by a CCD. A sample with a thin aluminum film bonded on the surface to reflect the laser is introduced in this CGS optical circuit. The aluminum film will deform based on the deformation of the sample and will result in different light path in this optical circuit. Therefore the interference fringe observed using the CCD can provide the strain field information of

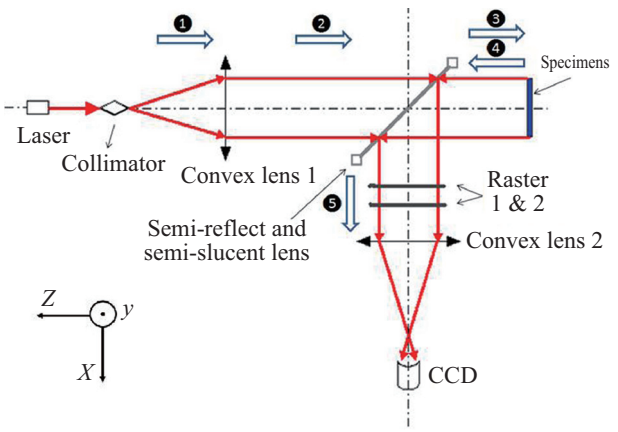


Fig. 1 Optical circuit of coherent gradient sensing method.

https://doi.org/10.1017/jmech.2016.114 Published online by Cambridge University Press

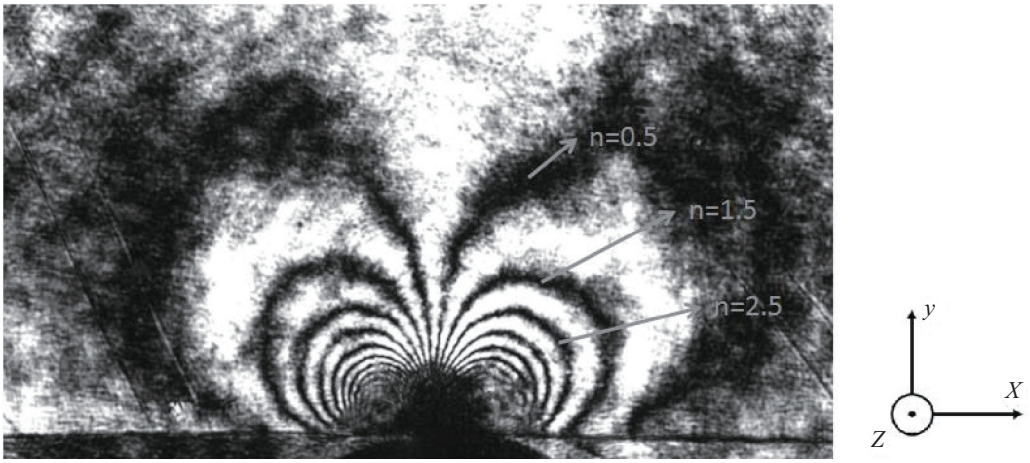


Fig. 2 Interference fringe at the load position using coherent gradient sensing method (n is order of interference fringe).

the sample surface using optical governing functions. The obtained interference fringe shape at the load position consists of a series of dark and light rings (as shown in Fig. 2). The size and shape of the dark/light rings can be used to detect the local strain field information at the microscale. The CGS method has a lot of advantages including 1) nondestructive, 2) easy to set up, 3) insensitive to surrounding vibration, 4) high accuracy, 5) can be used in on-site monitoring, and 6) can capture strain information in any position on material surface.

In this paper, the preparation process of a large scale FGM was introduced. The material properties including Young's modulus and density of this FGM were described using power-law functions. Subsequently, the optical governing function for the CGS method was derived. The CGS experimental results were discussed and compared with theoretical estimation.

2. PREPARATION OF FUNCTIONALLY GRADED MATERIAL

In this work, a large scale FGM filled with tiny glass spheres was prepared using gravity assisted casting technique. The dimension of the FGM sample is 100 mm × 40 mm × 6 mm. The material components of the FGM are listed in Table 1. The polymer is generated by mixing the epoxy resin and polyamide. The acetone works as thinner to completely mix the other components including epoxy resin, polyamide and glass spheres.

Table 1 Material component of the FGM

Component	Young's Modulus (GPa)	Poisson Ratio	Density (kg/m^3)	Weight percentage
Epoxy resin	1.4	0.35	1150	50%
Acetone	-	-	720	10%
Polyamide	-	-	860	25%
Glass sphere	70	0.23	2200	15%

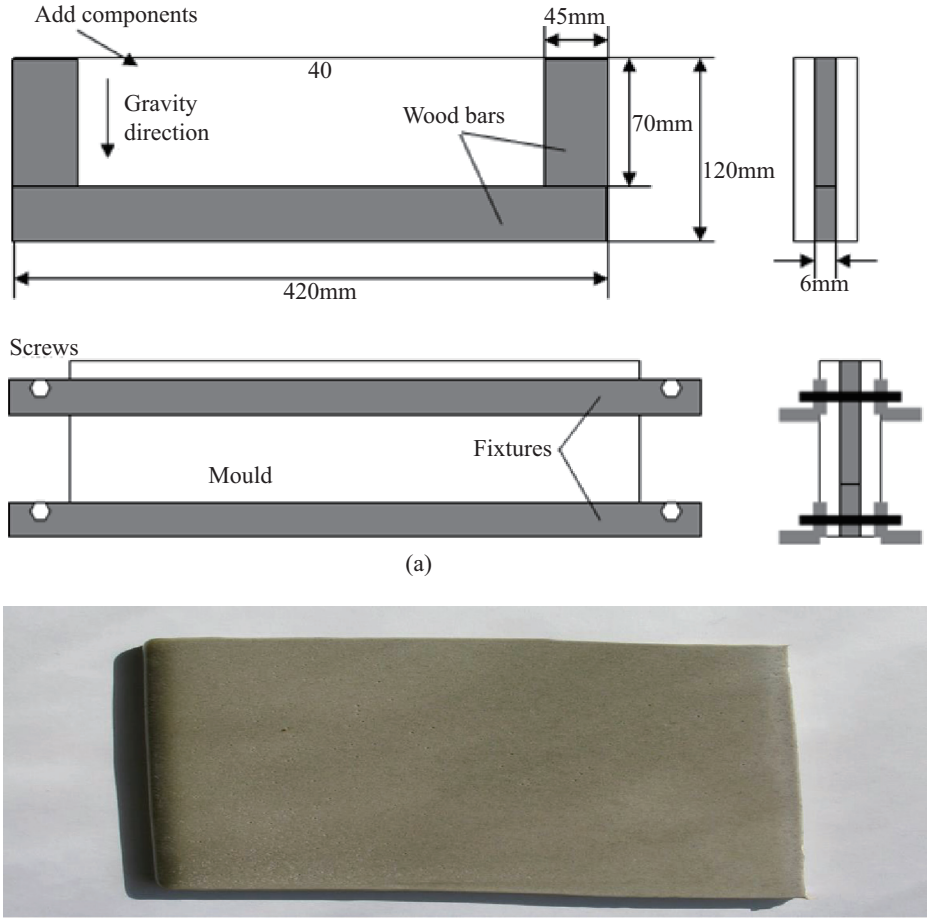
The weight percentage of Epoxy resin, Acetone, Polyamide and glass sphere are 50%, 10%, 25% and 15%, respectively. The weight percentage of components can influence the subsiding speed of the glass sphere. With different weight percentage of the components, the density of the mixture will be different. A higher density of liquid mixture will result in larger Buoyancy force acting on the glass sphere. This can slow down the subsiding speed of the glass sphere. Also, different percentage of Acetone, Epoxy Resin and Polyamide can also influence the hardening time of the mixture. This can be used to control the subsiding speed as well. The subsiding speed of glass sphere plays an important role in the gradient of FGM material properties in gravity direction. If the subsiding speed is too fast, most of the glass spheres will gather into clusters at the bottom of FGM; if the subsiding speed is too slow, the gradient of material properties is not large enough to generate 'large scale' FGM. In this study, the authors did a series of tests using different weight percentage of the components and conclude that the weight percentage used in this study (see Table 1) has the best performance.

The tiny glass spheres of diameter 70 μm play an important role in resulting in gradient material properties for FGM. Different glass sphere of diameter from 50 μm to 120 μm were considered in material preparation. In this range, the glass sphere of diameter 70 μm has best performance. The spheres with smaller diameter are easy to aggregate together to generate clusters and result in heterogeneous properties in the microscale. If the glass sphere size is too large, the FGM material cannot be considered as homogeneous in the macroscale. Based on these considerations, glass spheres with a diameter of 70 mm were selected in this study.

There are multiple steps to prepare the FGM:

1) Add acetone into epoxy resin at 50°C;
2) Add tiny glass balls into above mixture;
3) Keep stirring the mixture and add polyamide simultaneously;
4) Move the liquid mixture into the mould and keep it stable at room temperature; The mixture will turn into solid state after 48 hours;
5) Take out the sample from the mould and move it

https://doi.org/10.1017/jmech.2016.114 Published online by Cambridge University Press



(a)

(b)

Fig. 3 Preparation of FGM. (a) mould and fixture; (b) FGM sample.

into heater at 70°C for 4 hours.

During the solidation process, the tiny glass spheres will subside due to the higher density of glass ball compared with the liquid mixture. This will result in gradient varying density and stiffness of the FGM in gravity direction. The mould is composed of glass plates and wood bars (see Fig. 3a). The FGM sample prepared using the gravity assisted casting technique is shown in Fig. 3b.

The microstructure of FGM was observed to study the distribution of tiny glass spheres in the mixture in different heights (see Fig. 4). In Fig. 4, y represents the distance between the bottom of the sample and the measurement position. It shows that there is gradient distribution of glass sphere density. The glass sphere density is the highest at the bottom and the lowest at the top of the FGM sample. In the optical experiment design, a thin aluminum film of thickness 50 μm is bonded on the sample surface to reflect laser.

The power-law function is widely used to describe the gradient material property of FGM. In this study, the Young's modulus and density of FGM are described by power-law functions. Its Poisson ratio is considered to be consistent. The Young's modulus, density and Poisson ratio can be expressed as:

$$E = E_0 \cdot y^k \quad \rho = \rho_0 \cdot y^k \quad v = v_0 \tag{1}$$

where k is gradient coefficient, y is gradient direction, E_0, ρ_0 and v_0 are Young's modulus, density and Poisson ratio on top surface of FGM. When k is greater than zero, the material properties including Young's modulus and density keep increasing in y-direction. The FGM shows a positive gradient performance. When k is less than zero, the Young's modulus and density keep decreasing in y-direction. The FGM shows a negative gradient performance.

The material properties of this FGM including tensile modulus and density are measured along gradient direction. Fitting curves are generated using power-lawequations to describe Young's modulus and density variation in gradient direction, as shown in Eq.2 and Eq.3.

$$E = 2.5 \cdot y^{-0.1088} Gpa, v = 0.33 \tag{2}$$

$$\rho = 942.1 \cdot y^{-0.0689} \text{kg/m}^3 \tag{3}$$

where, y is the distance between measurement point and bottom of sample, ρ is material density, E is Young's modulus, and v is Poisson ratio. The power-lawequation based fitting curves of Young's modulus and density are shown in Fig. 5a and Fig. 5b.

The experimental data shows that both Young's modulus and density for this FMG prepared using gravity assisted casting technique increase in gradient direction.

https://doi.org/10.1017/jmech.2016.114 Published online by Cambridge University Press

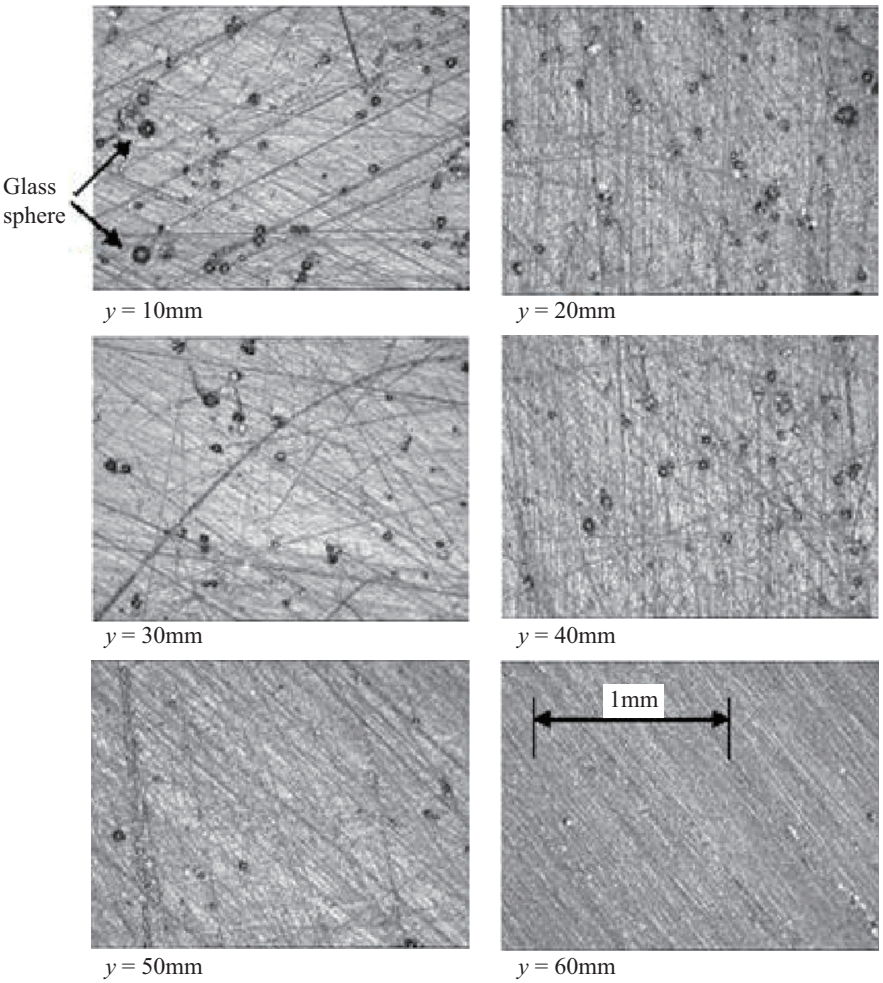


Fig. 4 Microstructure of FGM with glass ball filler at different height.

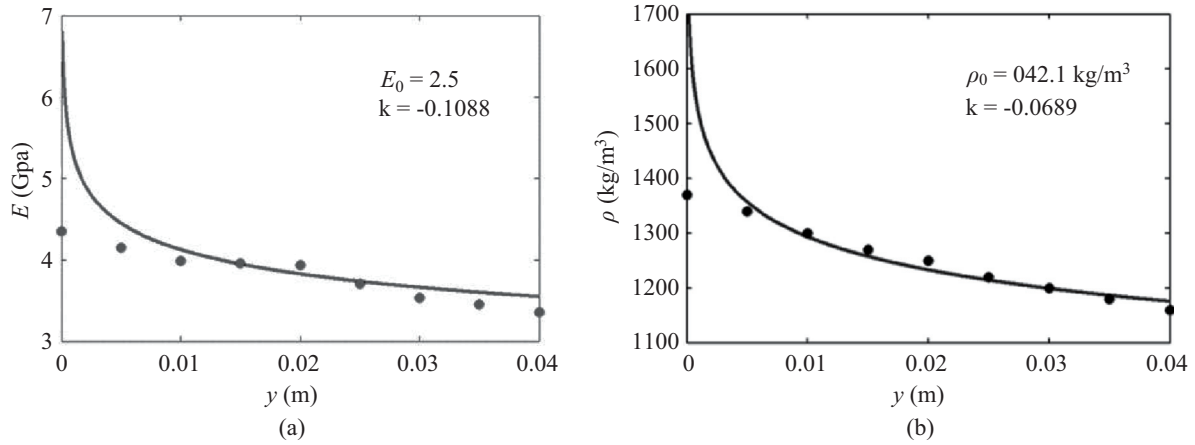


Fig. 5 Fitting curves and experimental data of (a) Modulus and (b) density.

The Young's modulus and density are larger at the positions closer to the sample bottom. The Young's modulus has a 30% difference within a distance of 40 mm in gradient direction. The Poisson ratio, which is equal to 0.33, is considered as a constant for FGM.

3. OPTICAL EXPERIMENTAL METHODS

A reflection based optical setup was designed because this FGM material is intransparent. In this work, the x-axis is horizontal direction and y-axis is vertical direction in sample plane, z-axis is out-of-plane direction of sample. Figure 1 shows the optical circuit in this work which is from top view (y-axis). The external load direction is gravity direction. For both gratings in this test, the principal direction of grating is parallel to x-axis, which is perpendicular to gravity direction. That means the grating line direction is parallel to y-axis, which is

https://doi.org/10.1017/jmech.2016.114 Published online by Cambridge University Press

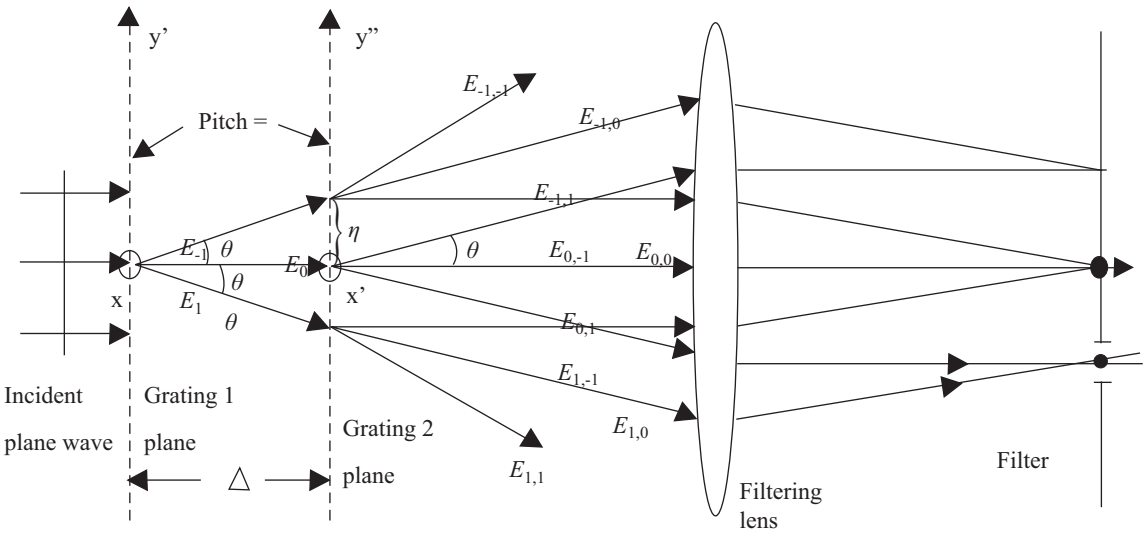


Fig. 6 Schematic relation between grating distance, pitch and orders of interference fringes.

gravity direction. There is a relation between grating distance, pitch and orders of interference fringes (see Fig. 6). The order and shape of the interference fringes can be used to indicate the material gradient and strain in this CGS method. The basic governing function of this optical experimental method can be described as [51]:

$$\frac{\partial w}{\partial y} = \frac{np}{2\Delta} \tag{4}$$

where w is the out-of-plane deflection of sample surface, n is order of interference fringes, p is grating pitch between neighbor lines, Δ is distance between the two gratings. The shift distance of diffraction light (on grating 2) diffracted by grating 1 can be described as:

$$\eta = \Delta \tan\varphi \approx \Delta\varphi \tag{5}$$

where, φ is diffraction angle and η is shift distance of diffraction light on grating 2 (see Fig. 6). The diffraction angle, which is also related to grating property, can be described as:

$$\varphi = \sin^{-1}\frac{\lambda}{p} \approx \frac{\lambda}{p} \tag{6}$$

where, λ is wavelength of the laser and p is grating pitch. In the light circuits shown in Fig. 1 and Fig. 6, the optical path length difference of two neighbor beams diffracted after the two gratings can be described as:

$$\delta S(x, y+\eta) - \delta S(x, y) = n\lambda \tag{7}$$

where, $\delta S(x, y)$ and $\delta S(x, y + \eta)$ represent the optical path lengths of two neighbor beams, respectively; n is order of interference fringes. Using Eqs. 5, 6 and 7, the relation between optical path length difference and order of interference fringes can be obtained:

$$\frac{\delta S(x, y+\eta) - \delta S(x, y)}{\eta} = \frac{n\lambda}{\eta} \tag{8}$$

Eq. 8 can also be described in differential format:

$$\frac{\partial\left[\delta S(x, y)\right]}{\partial y} = \frac{np}{\Delta} \tag{9}$$

Here, the item $\frac{\partial[\delta S(x, y)]}{\partial y}$ can be used to describe the sensitivity of CGS method. Based on Eq. 9, the sensitivity of CGS method can be improved with a longer distance between two gratings and smaller grating pitch. In this test, the distance between gratings is 50 mm.

Giannakopoulos and Suresh [60] proposed the out-of-plane deflection of FGM surface of which the material properties are described by power-law function under linear load:

$$w = \varepsilon_z \cdot \frac{d}{2} = -\frac{\upsilon \cdot (\tilde{\sigma}_r + \tilde{\sigma}_\theta)}{E} \cdot \frac{d}{2} = \frac{\upsilon \cdot d \cdot P}{4 I_k \cdot E_0} \cdot \frac{\cos(\beta \cdot \theta)}{r^{k+1} \cdot} \tag{10}$$

where, w is out-of-plane deflection of FGM surface, ε_z is strain in z direction (out-of-plane direction), d is FGM sample thickness, υ is Poisson ratio, $\tilde{\sigma}_r$ and $\tilde{\sigma}_\theta$ are stress components in r and θ directions in polar system, E is Young's modulus, P is linear load, k is gradient coefficient of FGM, β is a function of k and υ, and I_k is a function of k and β. From Eq. 4 and Eq. 10, the relationship between interference fringes and external linear load P:

$$P = -\frac{2E_0 \cdot I_k \cdot n \cdot p \cdot r^{k+2}}{\upsilon \cdot d \cdot \Delta \cdot \left[(k+1)\cos(\beta\theta)\cos\theta + \beta\sin(\beta\theta)\sin\theta\right]} \tag{11}$$

Here, the interference fringes information can be described by polar system coordinates r and θ, and interference fringe order n. Here the interference fringe order, n, can be either integer or integer plus 1/2. It represents light interference fringes when n is equal to integer (0, 1, 2 …). And it represents dark interference fringes when n is equal to integer plus 1/2 (0.5, 1.5, 2.5 …).

https://doi.org/10.1017/jmech.2016.114 Published online by Cambridge University Press

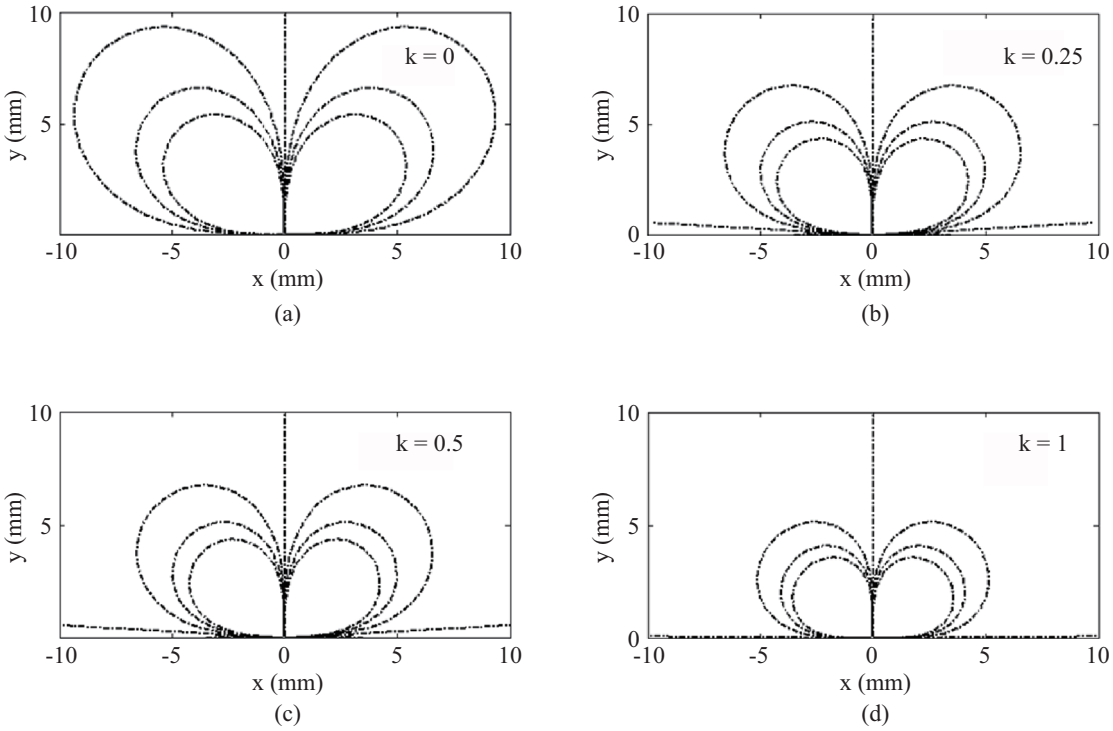


Fig. 7 Theoretical interference fringe shape of CGS method for FGM (k > 0)

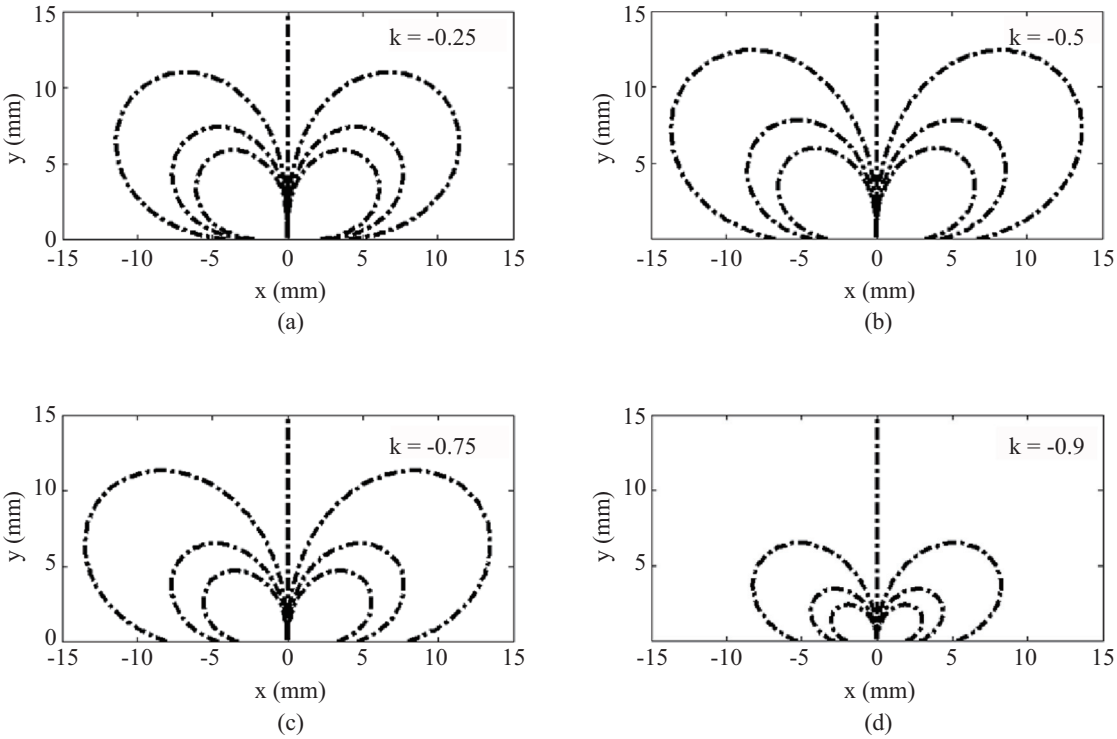


Fig. 8 Theoretical interference fringe shape of CGS method for FGM (k < 0)

The gradient of material properties of FGM will affect the shape of interference fringes of CGS method. The interference fringe shape of FGM can be determined by Eq. 11 with given external load, material properties and experimental configuration. For different gradient coefficient *k*, the interference fringe shapes were shown in Fig. 7 (k > 0) and Fig. 8 (k < 0). In this model, the external load is applied on top of FGM (gravity direction) and equal to 100N. The principal directions of both gratings are parallel to x-axis.

https://doi.org/10.1017/jmech.2016.114 Published online by Cambridge University Press

The theoretical results show that the interference fringes of CGS are symmetric to y-axis. It consists of a series of ringlike curves for each part. In Figs. 7 and 8, only the first four order of interference fringes were plotted (n = 0, 1, 2, and 3). The higher order of interference fringe is in inner part. When k is equal to 0, the zero order of the interference fringes coincide with x-axis and y-axis. When k is higher than zero, both parts of rings will move toward to the center line. And the size of interference fringe of the same order becomes smaller. When k is lower than zero, both parts of rings will move away from the center line. With a decreasing gradient coefficient k, the size of interference fringe gets bigger before k is equal to -0.5. After that, the size of rings gets smaller with a decreasing k.

4. RESULT AND DISCUSSION

The dimension of FGM samples is 100 mm × 40 mm × 6 mm, as shown in Fig. 9. The FGM gradient is in the gravity direction. An external load is applied on the top surface of the sample.

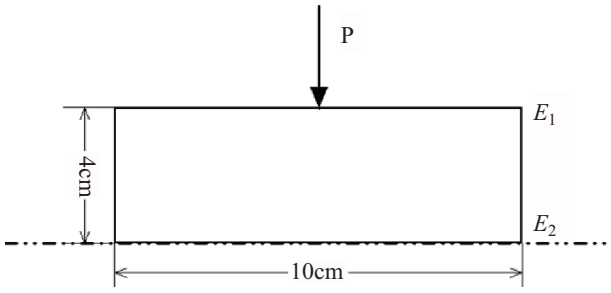


Fig. 9 Sample geometry and external load.

In this study, E_1 and E_2 represent the Young's modulus at the bottom and top of the FGM sample, respectively. With an inverse direction, the FGM sample can perform two different gradients, that is positive (k > 0) and negative (k < 0). The Young's modulus on top and bottom surfaces of the two samples is listed in Table 2. For sample 1, E_1 is less than E_2. The gradient Young's modulus can be described by Eq. 12 based on curve fitting. For sample 2, E_1 is greater than E_2. The gradient Young's modulus can be described by Eq. 13. Here y represent the height from the bottom of the sample (unit: m). The Poisson ratio is considered to be consistent (v = 0.33).

Table 2 Young's modulus of two FGM samples

(unit: GPa)	E_1	E_2
Sample 1	3.34	4.30
Sample 2	4.30	3.34

$$E = 6.0y^{0.1113} GPa \quad E_1 < E_2 \tag{12}$$

$$E = 2.5y^{-0.1008} GPa \quad E_1 > E_2 \tag{13}$$

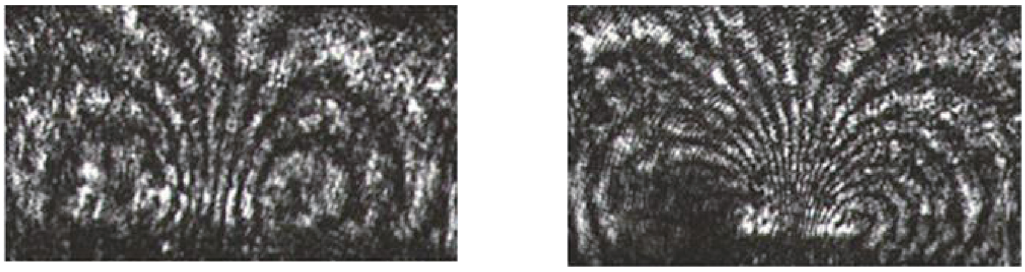
Based on optical-mechanical theory, the external linear load can be estimated using coordinates of each point in the interference fringe. In this study, multiple points in the interference fringes were collected to estimate the external load, which can be calculated using Eq. 11. Least square method was used to determine the average value of external load P. In this CGS test, the distance between the two gratings is 50 mm. The pitch of gratings is 25 μm. He-Ni laser with a 633 nm wavelength was used in this CGS experiment. The principal direction for both gratings is horizontal. The interference fringe of CGS test was captured by CCD and used to calculate the load applied on FGM in this study.

The CGS experiment result (Fig. 10) shows the similar interference fringe shapes as theoretical estimation (see Figs. 7 and 8). When $E_1 < E_2$, both parts of rings will move toward tocenter line. When $E_1 > E_2$, both parts of rings will move away from center line. The theoretical interference fringe shape plotted in Fig. 11 is obtained using Eq. 11. From Fig. 11, the same conclusion as observed in Fig. 10 can be obtained: when gradient coefficient k > 0 ($E_1 < E_2$), the interference fringes move toward to center line; when gradient coefficient k < 0 ($E_1 > E_2$), the interference fringes move away from center line. The shape of interference fringes from theoretical estimation (Fig. 11) matches well with that from CGS test (Fig. 10).

The CGS result also indicates higher load will result in high density of interference fringes. That means with an increasing load the interference fringes with the same order willbe larger. From Fig. 10, the interference fringe size with 200N external load is larger than that with 100N external load. It can also be observed that higher load (Figs. 10(b) and 10(d)) will result in higher-density interference fringes than lower load (Figs. 10(a) and 10(c)). This can also be validated using theoretical estimation using the governing function (Eq. 11): a higher load P will result in higher radius r for interference fringes with the same order n.

The operating load on FGM sample can be estimated using Eq. 11. In the test, the external force was implemented from 0 to 400N. Multiple points in the interference fringes with the same order were measured. The estimated external load and actual load are compared in Fig. 12. Both positive and negative gradient FGM samples were used for sensitivity study of the CGS test. The points on interference fringes with the order of 1.5 and 2.5 were measured and compared. Only the interference fringe with the order of 2.5 was used to estimate the external load based on result analysis. In Table 3, it is clear to conclude that the estimation using interference fringes with the order of 1.5 is not accurate enough. The error for order 1.5 is as high as 13.3% (for k < 0) and 19.6% (for k > 0). The error for order 2.5 can be reduced to 7.1% (for k > 0) and 7.3% (for k < 0). Therefore, only the interference fringes with the order of 2.5 were used to estimate the external load. The CGS method can be used to detect the external load in FGM with high accuracy.

https://doi.org/10.1017/jmech.2016.114 Published online by Cambridge University Press



(a) P = 100N, $E_1 < E_2$ (b) P = 200N, $E_1 < E_2$

(c) P = 100N, $E_1 > E_2$ (d) P = 200N, $E_1 > E_2$

Fig. 10 Interference fringes in CGS test for FGM.

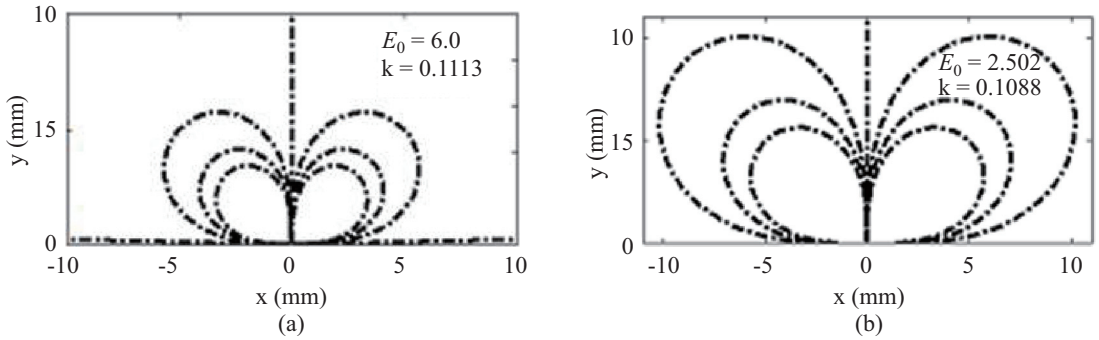


Fig. 11 Theoretical interference fringe shape of CGS method for FGM (P = 100N) when (a) k = 0.1113 and (b) k = -0.1088.

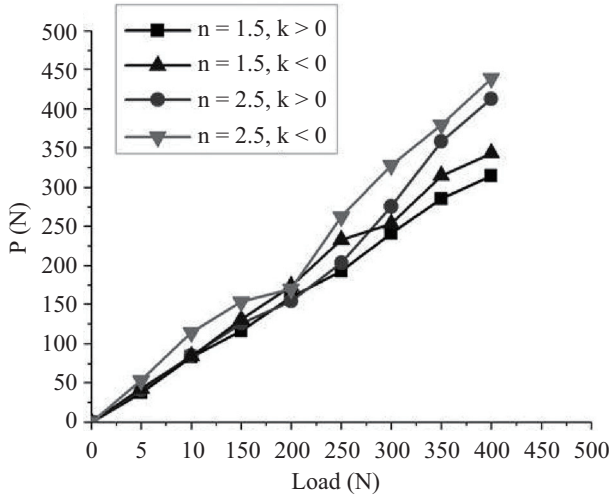


Fig. 12 Comparison between the estimated load (P) using CGS method and the operating load.

Table 3 Average error between load estimation using CGS method and operating load

Interference fringe order n and gradient coefficient k	Average error
n = 1.5, k > 0	19.6%
n = 1.5, k < 0	13.3%
n = 2.5, k > 0	7.1%
n = 2.5, k < 0	7.3%

The error in the CGS method can be attributed to several possible reasons. First of all, the external load applied on the sample surface is considered to be a line load in the governing function. But the contact surface between the indenter and sample surface in this test cannot be a line because of the limitation of the indenter size. This will result in some errors in the final results. Also, in the optical circuit setting the accuracy of the dimensions in the optical circuit, such as the distance between lens and sample, will introduce some errors in the exter-

https://doi.org/10.1017/jmech.2016.114 Published online by Cambridge University Press

nal load calculation. Besides that, the polyacrylamide material might be inhomogeneous locally at the load point at the microscale. The minor difference of actual material properties around load point and the material properties used in the governing function may result in some errors. Finally, the accuracy of the measurement of the interference fringe size can result in error as well. In the measurement, the radius of dark interference fringes (n = 1.5, 2.5, …) was used to estimate the load. Both the outer and inner boundaries of interference fringes shouldbe measured to calculate the average radius. For lower order interference fringe (n = 0.5 and 1.5), the width of interference fringe (distance between outer and inner boundaries) is larger. Moreover, for lower order interference fringes, the boundaries are more ambiguous to observe. This can also explain that the error is reduced using a higher order of interference fringes to estimate the load (see Table 3). Overall, the error between estimated load and operating load can be further reduced by using sharper intender, setting more accurate optical circuit, preparing high quality materials and measuring higher order of interference fringes. In consideration of those factors, the load estimation error (< 8%) using order 2.5 is acceptable.

There are several advantages of the CGS method to detect external load. First, the CGS method is nondestructive. The test is all based on optical circuit. There are no sensors planted inside or glued on the surface of the sample. So no damage or destruction is involved in the tested material. This provides the possibility to apply this novel optical methodology in the structural health monitoring to detect crack propagation in metallic and composite structures, which can be potentially implemented into airframe structures. Another advantage of the CGS method is this methodology is easy to set up. In the optical circuit, only one laser generator, two convex lens, and one CCD are required. There is low requirement on the environment conditions like temperature and humidity. Finally, the governing function to estimate the external force is straightforward. The only input parameter to obtain the load is the CGS interference size. Therefore it is potential to be used in on-site monitoring and damage estimation.

5. CONCLUSIONS

In this paper, a large scale FGM was designed and prepared using gravity assisted casting technique. Tiny glass balls with a diameter of 70 μm were filled in this FGM to introduce the gradient material properties. Both the Young's modulus and density have a 30% difference within a distance of 40 mm in gradient direction. The Young's modulus and density of the FGM can be described by power-lawfunctions. A reflection based optical circuit was designed for CGS test and the optical mechanical governing function was derived. This governing function can be used to describe the relation between interference fringes and load/stress. The CGS experiment result match well with theoretical estimation. The operating load on FGM sample can be calculated using information of interference fringes. This CGS method as a nondestructive methodology can be used to detect the damage in FGM with high accuracy.

REFERENCES

1. Vinay, N., Gu, H. and Yu, C., "Monte Carlo simulation for investigating influence of junction and nanofiber properties on electrical conductivity of segregated-network nanocomposites," *Acta Materialia*, **59**, pp. 4548-4555 (2011).
2. Gu, H., Gao, X. and Li, X., "Molecular Dynamics Study on Mechanical Properties and Interfacial Morphology of an Aluminum Matrix Nanocomposite Reinforced by Silicon Carbide Nanoparticles," *Journal of Computational and Theoretical Nanoscience*, **6**, pp. 61-72 (2009).
3. Zhang, J., *et al*., "A novel statistical spring-bead based network model for self-sensing smart polymer materials," *Smart Materials and Structures*, **24**, 085022 (2015).
4. Zhang, J., Koo, B., Subramanian, N., Liu, Y. and Chattopadhyay, A., "An optimized cross-linked network model to simulate the linear elastic material response of a smart polymer," *Journal of Intelligent Material Systems and Structures*, DOI: 1045389X15595292 (2015).
5. Wang, H., Hu, Z., Lu, W. and Thouless, M. D., "A mechanism-based framework for the numerical analysis of creep in zircaloy-4," *Journal of Nuclear Materials*, **433**, pp. 188-198 (2013).
6. Hu, Z., Lu, W. and Thouless, M. D., "Slip and wear at a corner with Coulomb friction and an interfacial strength," *Wear*, **338**, pp. 242-251 (2015).
7. Ma, X. and Shi, H., "On the fatigue small crack behaviors of directionally solidified superalloy DZ4 by in situ SEM observations," *International Journal of Fatigue*, **35**, pp. 91-98 (2012).
8. Ma, X., Duan, Z., Shi, H., Murai, R. and Yanagisawa, E., "Fatigue and fracture behavior of nickel-based superalloy Inconel 718 up to very high cycle regime," *Journal of Zhejiang University-Science A*, **11**, pp. 727-737 (2010).
9. Zhang, J., Gu, J., Li, L., Huan, Y. and Wei, B., "Bonding of alumina and metal using bulk metallic glass forming alloy," *International Journal of Modern Physics B*, **23**, pp. 1306-1312 (2009).
10. Peng, Y. and Zhou, D., "Stress Distributions Due to a Concentrated Force on Viscoelastic Half-Space," *Journal of Computations & Modelling*, **2**, pp. 51-74 (2012).
11. Atkinson, C. and List, R. D., "Steady state crack propagation into media with spatially varying elastic properties," *International Journal of Engineering Science*, **16**, pp. 717-730 (1978).
12. Delale, F. and Erdogan, F., "The crack problem for a nonhomogeneous plane," *Journal of Applied Me-*

https://doi.org/10.1017/jmech.2016.114 Published online by Cambridge University Press

chanics, **50**, pp. 609-614 (1983).

13. Eischen, J. W., "Fracture of nonhomogeneous materials," *International Journal of Fracture*, **34**, pp. 3-22 (1987).
14. Huang, G., Wang, Y. and Yu, S., "Fracture analysis of a functionally graded interfacial zone under plane deformation," *International Journal of Solids and Structures*, **41**, pp. 731-743 (2004).
15. Chalivendra, V. B., Shukla, A. and Parameswaran, V., "Quasi-static stress fields for a crack inclined to the property gradation in functionally graded materials," *Acta Mechanica*, **162**, pp. 167-184 (2003).
16. Parameswaran, V. and Shukla, V., "Crack-tip stress fields for dynamic fracture in functionally gradient materials," *Mechanics of Materials*, **31**, pp. 579-596 (1999).
17. Marur, P. R., "Tippur H V. Evaluation of mechanical properties of functionally graded materials," *Journal of Testing and Evaluation*, **26**, pp. 539-545 (1998).
18. Butcher, R. J., Rousseau, C. E. and Tippur, H. V., "A functionally graded particulate composite: preparation measurements and failure analysis," *Acta Materials*, **47**, pp. 259-268 (1999).
19. Parameswaran, V. and Shukla, A., "Processing and characterization of a model functionally gradient material," *Journal of Material Science*, **35**, pp. 21-29 (2000).
20. Yao, X. F., Xiong, T. C., Xu, W. and Yeh, H.Y., "Experimental investigations on deformation and fracture behavior of glass sphere filled epoxy functionally graded materials," *Applied Composite Materials*, **13**, pp. 407-420 (2006).
21. Yao, X. F., Yeh, H. Y. and Chen, X. B., "Visualization of crack tip behaviour in functionally gradient materials using coherent gradient sensing (CGS)," *Modelling and Simulation in Materials Science and Engineering*, **13**, pp. 621 (2005).
22. Yao, X. F., Liu, D. L., Xu, H. M. and Yeh, H. Y., "Investigation of fracture characterizations of functionally graded materials," *Fatigue & Fracture of Engineering Materials & Structures*, **32**, pp. 148-158 (2009).
23. Hu, Z., Lu, W., Thouless, M. D. and Barber, J.R., "Simulation of wear evolution using fictitious eigenstrainsm," *Tribology International*, **82**, pp. 191-194 (2015).
24. Neerukatti, R. K., Hensberry, K., Kovvali, N. and Chattopadhyay, A., "A novel probabilistic framework for damage localization and prognosis including temperature compensation," *Journal of Intelligent Material Systems and Structures*, **27**, pp. 592-607 (2015).
25. He, J. and Yuan, F. G., "Lamb-wave-based two-dimensional areal scan damage imaging using reverse-time migration with a normalized zero-lag cross-correlation imaging condition," *Structural Health Monitoring*, 1475921716674373 (2016).
26. Ye, J., *et al*., "Statistical Impact-Echo Analysis Based on Grassmann Manifold Learning: Its Preliminary Results for Concrete Condition Assessment," *EWSHM-7th European Workshop on Structural Health Monitoring*, Nantes, France (2014).
27. Ye, J., *et al*., "Noise Reduction Methods for Hammering Impact Acoustic Inspection: An Experimental Comparison," *Structural Health Monitoring*, DOI: 10.12783/SHM2015/151 (2015).
28. Li, Z. and Gu, H., "A Fixed Platform Topside Piping System Strength Analysis Under Dynamic Pigging/Slugging Loads," *American Journal of Civil Engineering*, **4**, pp. 216-224 (2016).
29. Li, Z., Wu, Y. and Cui, W., "Finite element method based structural optimization for SWATH," *Journal of Ship Mechanics*, **9**, pp. 99-108 (2005).
30. Tan, L., Acharya, A. and Dayal, K., "Coarse variables of autonomous ODE systems and their evolution," *Computer Methods in Applied Mechanics and Engineering*, **253**, pp. 199-218 (2013).
31. Peng, T., Saxena, A., Goebel, K., Xiang, Y. and Liu, Y., "Integrated experimental and numerical investigation for fatigue damage diagnosis in composite plates," *Structural Health Monitoring*, DOI: 1475921714532992 (2014).
32. Hu, Z., Lu, W., Thouless, M. D. and Barber, J. R., "Effect of plastic deformation on the evolution of wear and local stress fields in fretting," *International Journal of Solids and Structures*, **82**, pp. 1-8 (2016).
33. Liu, Y., Huang, J., Yang, B., Sumpter, B.G. and Qiao, R., "Duality of the interfacial thermal conductance in graphene-based nanocomposites", *Carbon*, **75**, pp. 169-177 (2014).
34. Liu, Y., Hu, C., Huang, J., Sumpter, B. G. and Qiao, R., "Tuning interfacial thermal conductance of graphene embedded in soft materials by vacancy defects," *The Journal of Chemical Physics*, **142**, 244703 (2015).
35. Zhang, J., Liu, K., Luo, C. and Chattopadhyay, A., "Crack initiation and fatigue life prediction on aluminum lug joints using statistical volume element-based multiscale modeling," *Journal of Intelligent Material Systems and Structures*, **24**, pp. 2097-2109 (2013).
36. Zhang, J., Johnston, J. and Chattopadhyay, A., "Physics-based multiscale damage criterion for fatigue crack prediction in aluminium alloy," *Fatigue & Fracture of Engineering Materials & Structures*, **37**, pp. 119-131 (2014).
37. Tan, L., Acharya, A. and Dayal, K., "Modeling of slow time-scale behavior of fast molecular dynamic systems," *Journal of the Mechanics and Physics of Solids*, **64**, pp. 24-43 (2014).
38. Tan, L. and Bhattacharya, K., "Length scales and pinning of interfaces," *Philosophical Transactions of the Royal Society A*, **374**, 20150167 (2016).
39. Gu, H., Wang, J. and Yu, C., "Three-dimensional Modeling of Percolation Behavior of Electrical

https://doi.org/10.1017/jmech.2016.114 Published online by Cambridge University Press

Conductivity in Segregated Network Polymer Nanocomposites Using Monte Carlo Method," *Advances in Materials*, **5**, pp. 1-8 (2016).

40. Gu, H., Wang, J. and Li, Z., "Molecular Dynamics Simulation of Tensile Behavior on Ceramic Particles Reinforced Aluminum Matrix Nanocomposites," *International Journal of Materials Science and Applications*, **5**, pp. 151-159 (2016).
41. Neerukatti, R. K., Yekani, F. M. and Chattopadhyay, A., "Gaussian process-based particle filtering approach for real-time damage prediction with application," *Journal of Aerospace Engineering*, DOI: 10.1061/(ASCE)AS.1943-5525.0000680 (2016).
42. Neerukatti, R. K., Liu, K. C., Kovvali, N. and Chattopadhyay, A., "Fatigue life prediction using hybrid prognosis for structural health monitoring," *Journal of Aerospace Information Systems*, **11**, pp. 211-232 (2014).
43. He, J. and Yuan, F., "Damage Identification for Composite Structures using a Cross-Correlation Reverse-Time Migration Technique," *Structural Health Monitoring*, **14**, pp. 558-570 (2015).
44. He, J. and Yuan, F., "Lamb wave-based subwavelength damage imaging using the DORT-MUSIC technique in metallic plates," *Structural Health Monitoring*, **15**, pp. 65-80 (2016).
45. Xu, Q., *et al*., "Robust self-cleaning and micromanipulation capabilities of gecko spatulae and their bio-mimics," *Nature Communications*, **6**, DOI: 10.1038/ncomms9949 (2015).
46. Liu, Y., Huxtable, S. T., Yang, B., Sumpter, B. G. and Qiao, R., "Nonlocal thermal transport across embedded few-layer graphene sheets," *Journal of Physics: Condensed Matter*, **26**, 502101 (2014).
47. Cai, W. and Gouveia, L. L., "Modeling and simulation of maximum power point tracker in Ptolemy," *Journal of Clean Energy Technologies*, **1**, pp. 6-9 (2013).
48. Cai, W., Chan, J. and Garmire, D., "3-Axes MEMS Hall-Effect Sensor," *2011 IEEE Sensors Applications Symposium*, pp. 141-144 (2011).
49. Peng, T., Saxena, A., Goebel, K., Xiang, Y., Sankararaman, S. and Liu, Y., "A novel Bayesian imaging method for probabilistic delamination detection of composite materials," *Smart Materials and Structures*, **22**, 125019 (2013).
50. He, J. and Yuan, F., "An enhanced CCRTM (E-CCRTM) damage imaging technique using a 2D areal scan for composite plates," *SPIE Smart Structures/NDE 2016*, Las Vegas, NV, USA (2016).
51. Tippur, H. V., Krishnaswamy, S. and Rosakis, A. J., "A coherent gradient sensor for crack tip deformation measurements: analysis and experimental results," *International Journal of Fracture*, **48**, pp. 193-204 (1991).
52. Bruck, H. A. and Rosakis, A. J., "On the sensitivity of CGS: Part I-A theoretical investigation of accuracy in fracture mechanics applications," *Optics and Lasers in Engineering*, **17**, pp. 83-101 (1992).
53. Bruck, H. A. and Rosakis, A. J., "On the sensitivity of CGS: Part II-An experimental investigation of accuracy in fracture mechanics applications," *Optics and Lasers in Engineering*, **18**, pp. 25-51 (1993).
54. Lee, Y. J., Lambros, J. and Rosakis, A., "Analysis of coherent gradient sensing (CGS) by Fourier optics," *Optics and Lasers in Engineering*, **25**, pp. 25-53 (1996).
55. Wang, J., Phillion, A. B. and Lu, G., "Development of a visco-plastic constitutive modeling for thixoforming of AA6061 in semi-solid state," *Journal of Alloys and Compounds*, **609**, pp. 290-295 (2014).
56. Wang, J., Brabazon, D., Phillion, A. B. and Lu, G., "An innovative two-stage reheating process for wrought aluminum alloy during thixoforming," *Metallurgical and Materials Transactions A*, **46**, pp. 4191-4201 (2015).
57. Yao, X. F., Yeh, H. Y. and Xu, W., "Fracture investigation at V-notch tip using coherent gradient sensing (CGS)," *International Journal of Solids and Structures*, **43**, pp.1189-1200 (2006).
58. Yao, X. F., Xu, W. and Yeh, H. Y., "Improvement of measurement error for modified coherent gradient sensing," *Measurement Science and Technology*, **17**, pp. 1491-1495 (2006).
59. Yao, X. F., Xu, W. and Yeh, H. Y., "Fracture visualization using hybrid optical technique combining coherent gradient sensing (CGS) with caustics," *Measurement Science and Technology*, **16**, 2357 (2006).
60. Giannakopoulos, A. E. and Suresh, S., "Indentation of Solids with gradients in elastic properties," *Internatinal Journal of Solids and Structures*, **34**, pp. 2357-2392 (1997).

(Manuscript received August 3, 2016,
accepted for publication October 23, 2016.)

https://doi.org/10.1017/jmech.2016.114 Published online by Cambridge University Press